



Wall pressure fluctuations in rectangular partial enclosures



T. Pagliaroli*, R. Camussi

Department of Engineering, University Roma Tre, via della Vasca Navale 79, 00146 Roma, Italy

ARTICLE INFO

Article history:

Received 5 June 2014

Received in revised form

29 October 2014

Accepted 3 December 2014

Handling Editor: P. Joseph

Available online 7 January 2015

ABSTRACT

Wall pressure fluctuations generated within rectangular partial enclosures (RPEs) have been studied experimentally for a broad range of geometrical parameters. The geometry represents a simplified version of a new generation trapped vortex combustor and consisted of a rectangular cavity connected to a neck of smaller size. Wall pressure fluctuations have been measured through wall mounted microphones providing single and multi-variate pressure statistics both in the physical space and in the Fourier domain. In order to interpret the pressure signals, aerodynamic and acoustic investigations have been carried out as well for several cavity–neck ratios. The analysis of the acoustic response of the cavity has been conducted both numerically and experimentally and a simple theoretical model has been proposed to predict the frequency of the acoustic resonances. The aerodynamic study has been carried out through PIV measurements that provided characterization in terms of the geometrical parameters of both the large-scale vortex generated within the cavity and the recirculation zone formed upstream of the neck. The use of the POD decomposition permitted us to correlate the dynamics of the recirculation with the observed pressure statistics. The aerodynamic and acoustic investigations allowed us to interpret exhaustively the wall pressure cross-statistics and to separate contributions induced by hydrodynamic and purely acoustic pressure fluctuations.

© 2014 Elsevier Ltd. All rights reserved.

1. Introduction

Rectangular partial enclosures (hereafter denoted as RPEs), also named rectangular covered cavities, are encountered in many industrial applications including heating, ventilation and air conditioning. In many industrial systems, RPEs are installed to control heat losses, to provide convective flow partitioning and to suppress aerodynamic noise [1]. The main drawback in the use of RPEs is the generation of pressure oscillations that might induce structural vibrations and consequent mechanical failures [2]. Pressure oscillations generated by the coupling of a flow with acoustic standing waves are commonly called *self-sustained* or *self-excited oscillations*. This phenomenon was widely investigated in the literature in T-joints, safety valves, pipes with side branches and open cavities. Typically, the interaction of a shear layer with the walls has been identified as the main source of acoustic waves [3–6]. Several observations have suggested that the pressure oscillations induced by aerodynamic noise into RPEs generally fall into two categories, depending on whether the incoming jet flow is free or bounded on one side [7–9], the latter category being the most frequent in practice.

Recently, the interest for RPEs has been renewed thanks to their application in the field of combustion in particular in the design of the so-called trapped vortex combustors (TVCs) [10–12]. In this combustor, a vortex is trapped into a cavity, this

* Corresponding author.

E-mail address: tiziano.pagliaroli@gmail.com (T. Pagliaroli).

configuration being beneficial for the generation of a stable flame and an efficient combustion. Despite combustion stability being cited as a relevant characteristic of TVC, Hsu et al. [13] identified a combustion instability in which the flame blow-out was preceded by flame intermittency and tonal noise emission. More recently Agarwal et al. [14] pointed out that the acoustic depth-mode of the cavity is dominant in this kind of combustors and it influences the heat release. Gutmark et al. [15] notice that TVC is susceptible to the onset of combustion oscillations in pressure and heat release. They have shown that OH^* chemiluminescence fluctuations and pressure are tonal and isofrequentual, for specific operative conditions.

Understanding and predicting acoustic instability in combustion chamber requires the knowledge of the acoustic behavior of the geometry. Despite the aerodynamic behavior of RPEs being studied extensively in the literature, much lesser studies have been focalized on the characterization of the pressure field, and of the statistics of the wall pressure fluctuations. The main objective of the research presented herein is to provide a complete description of the pressure fluctuations induced in a RPE, representing a simplified version of a real TVC in non-reactive conditions. More specifically, significant geometrical simplifications have been applied to the transverse direction to make the resulting flow treatable by planar Particle Image Velocimetry. The resulting geometry enables a fundamental study in the flow instability mechanism affecting a spanwise-constrained flow. In fact a more important three-dimensional motion is expected both in large width-to-depth ratio and in axisymmetric combustor geometries.

The problem was studied experimentally and for several geometrical parameters. Velocity fields were determined through the Particle Image Velocimetry (PIV) technique providing an overall picture of the aerodynamic behavior. The acoustic response of the cavity was analyzed both numerically and experimentally, whereas the wall pressure fluctuations in the presence of the mean flow were measured using wall mounted microphone arrays. The post-processing data have included the application of the proper orthogonal decomposition (POD) to the PIV fields and the estimation of the cross-statistics (cross-correlations and cross-spectra) of the wall pressure fluctuations.

A description of the experimental set-ups investigated is given in Section 2, while the preliminary aerodynamic and acoustic characterization of the RPE are presented in Section 3 and 4 respectively. Section 5 includes the main results mainly consisting of the wall pressure fluctuation statistics, whereas conclusions are presented in Section 6.

2. Experimental set-up

2.1. Test case and flow conditions

Several experiments have been performed for obtaining a phenomenological overview of the self-excited pressure oscillations in a RPE. In Fig. 1 a sketch of the test case is presented. The analyzed geometry represents a simplified version of a so-called third generation Trapped Vortex Combustors that are typically characterized by a large deep cavity, and air or fuel injectors positioned on one side of it [12,14]. In order to modify the main geometrical parameters, the cavity length, L , was kept fixed whereas the depth, D , was varied by inserting plates on the cavity bottom, so that the cavity aspect ratio can be defined as $\Gamma = D/d$, where d is the transversal length of the neck. Although in the present study, Γ could be changed from 2.00 to 7.3, particular attention has been given to three geometrical conditions: $\Gamma = 3.8$, also named *square cavity*, $\Gamma = 3.2$ named *rectangular cavity A* and $\Gamma = 2.6$, named *rectangular cavity B* (see Table 1). As illustrated in the following, the cavity aspect ratio plays a fundamental role in terms of flow-structure, pressure gradient, acoustic and aeroacoustic behavior. The number of the achievable geometrical configurations is 72, but the following discussions are restricted to the most interesting cases. In Table 2 all values assumed by the geometrical parameters are summarized. The geometry analyzed is characterized by a width (W)-to-length (L) ratio equal to 0.33. The flow in the narrow-span rectangular cavities, $W/L < 1$, is two-dimensional. This assumption, according to the results carried out by [16], has been further confirmed by several RANS

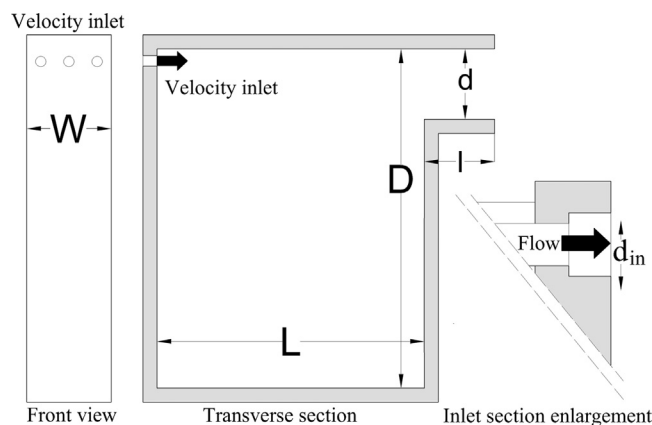


Fig. 1. Sketch of the frontal and the transverse view of the test case and enlargement of the inlet section. The main geometrical parameters are also reported for clarity.

Table 1Sketch of three RPEs on which the experimental investigation is focused, for all of these configurations $W=60$ mm and $d=50$ mm.



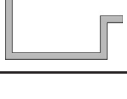
Configuration	Γ	D (mm)	Geometry
Square cavity	3.8	190	
Rectangular cavity A	3.2	160	
Rectangular cavity B	2.6	130	

Table 2

Range of values of the test case geometrical parameters.

Γ	D (mm)	L (mm)	W (mm)	l (mm)	d (mm)	d_{in} (mm)
2–7.3	100–220	190	60	50	30–50	7

and URANS simulations that have been carried out by the authors and that are not reported here for brevity. As rendered in Fig. 1, the air is injected into the test case through the three circular inlets that are 7 mm in diameter (d_{in}). The jet mass-flow rates range from 7 g/s to 15 g/s, for a corresponding bulk velocity inlet of 50 and 108 m/s. Taking into account the bulk inlet velocity, U_{in} , the jet Reynolds number follows

$$Re = \frac{U_{in} d_{in}}{\nu}, \quad (1)$$

for the mass-flow values under investigation, the Reynolds number interval is $2 \times 10^4 < Re \leq 5 \times 10^4$. These Re numbers ensure low-frequency acoustic wave emissions within the region 1.2 and 2.5 jet diameters [17,18]. Such perturbations excite the RPE first modes, ensuring the achievement of the self-excited oscillations.

2.2. Air supply system

The facility investigated herein has been designed to carry out experiments at atmospheric pressure. The air supply consists of two lines: the first one connects an high pressure plenum chamber to the test rig through a series of ball valves, pressure regulators and flow meters. The second one, denoted as *bypass* line, is connected to the PIV seeding system described in the next paragraph. The air supply system is depicted in Fig. 2 by a single-line diagram. The flow-meter adopted to regulate the mass-flow is a Brooks Smart Mass Flow 5853S. The flow-meter is connected to a home-made *muffler-collector* very similar to the one proposed by [19]. It is designed in a single-inlet/triple-outlet configuration, to split the main mass-flow in three equivalent flows. The *muffler-collector* is filled with an acoustic absorbing foam in order to damp the narrow-band tonal noise generated in the air supply system (see Fig. 3). Several measurements have been performed to verify the homogeneity of the mass-flow at the outlets of the collector and to verify the effectiveness of the acoustic damping provided by the muffler. For the sake of conciseness, these results, satisfactory in all cases, are not reported herein.

2.3. Particle Image Velocimetry

The cavity investigated is equipped with three optical accesses, the top, bottom and side walls, suitable for the application of the PIV measurement technique. A scheme of the PIV set-up is given in Fig. 4(a). The PIV system consists of a PCO Sensicam (double shutter camera, 1280×1024 resolution) and a 2 mm thick laser sheet created by a double cavity Nd: YAG laser (Big Sky Laser/Quantel 200 mJ light pulses). Each pair of acquired images has been processed using the software PIVdef, developed by researchers of the Italian Ship Model Basin – CNR center [20]. The post-processing procedure uses iterative adaptive correlations and windows deformation algorithms. The resolution of the interrogation area has been varied from 64×64 pixels to 16×16 pixels with 50 percent overlap. After each iteration, the vector map has been filtered to remove spurious vectors, identified by median tests and replaced using 2D interpolations. Eventually, a peak locking analysis, based on the displacement probability density function (PDF), has confirmed the proper setting of the final iteration. The time delay between two consecutive laser pulses has been adjusted from 50 μ s to 150 μ s to provide a mean displacement vector of about 5 pixels and a velocity uncertainty of 1–2 percent. This accuracy is referred to all flow conditions investigated. The image pair acquisition rate was 5 Hz. A seeding spray of DEHS (DiEthylHexylSebacate)

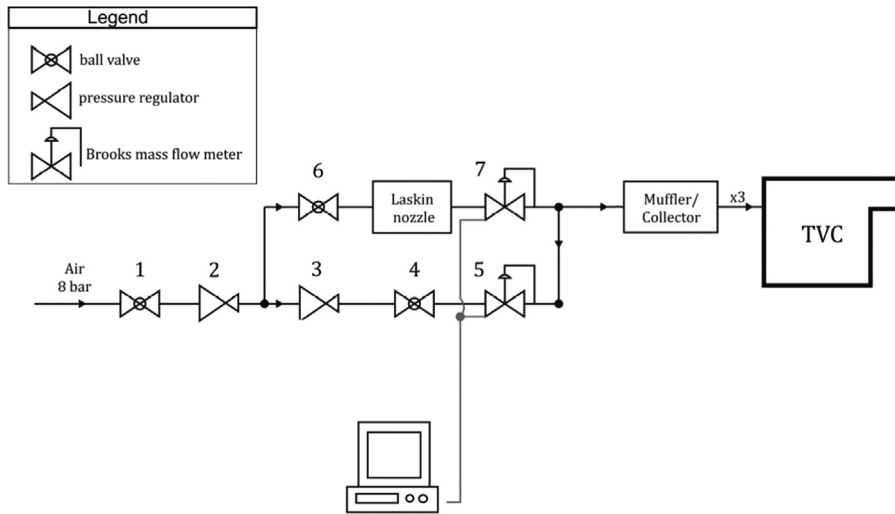


Fig. 2. Single-line diagram of the feedline system.

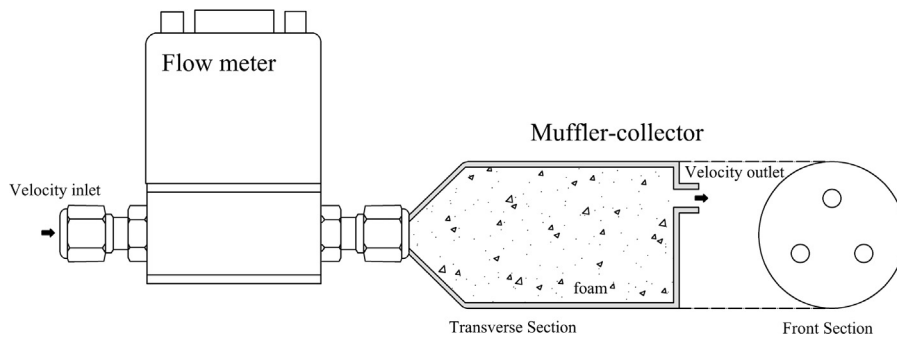


Fig. 3. Conceptual design of the muffler-collector device.

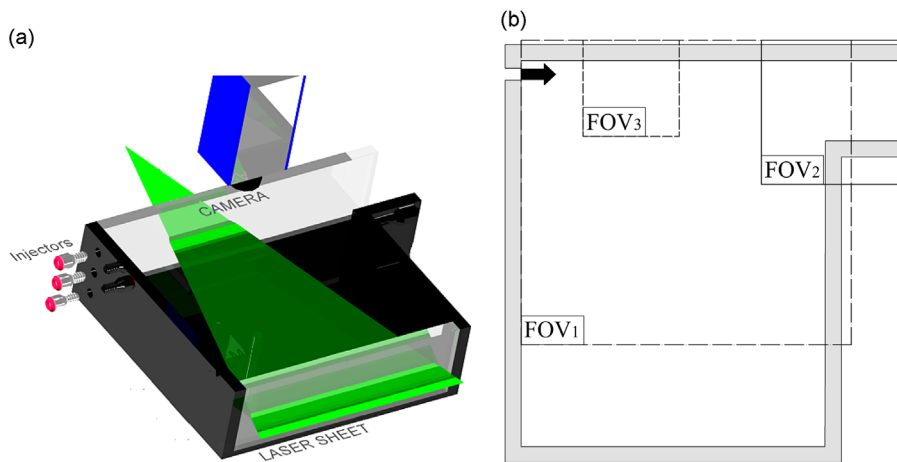


Fig. 4. Three dimensional scheme of the PIV experimental set-up (a). Sketch of the three different FOV investigated (b).

characterized by $1\ \mu\text{m}$ diameter particles has been produced by a PivTec Laskin nozzle. The seeding was mixed with the main stream air and subsequently injected into the muffler as shown in Fig. 2. Essentially, three fields of view (FOV) have been investigated: the first one, denoted as FOV₁, is $190 \times 190\ \text{mm}^2$ wide and covers almost the whole cavity; the second one, named FOV₂, is $90 \times 90\ \text{mm}^2$ wide and is centered on the neck; the last one, denoted as FOV₃ and $60 \times 60\ \text{mm}^2$ wide, is centered on the top wall of the RPE. A scheme of the three FOV is reported in Fig. 4(b).

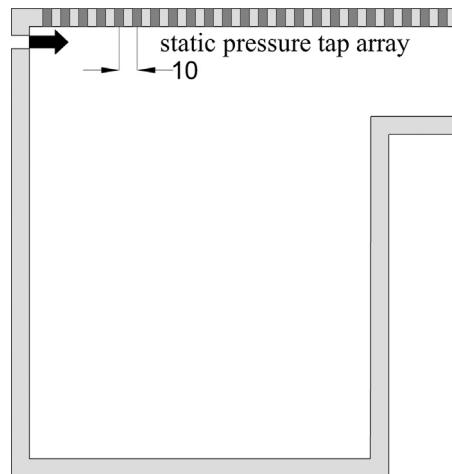


Fig. 5. Sketch of the static pressure taps positioned on the top wall of the RPE.

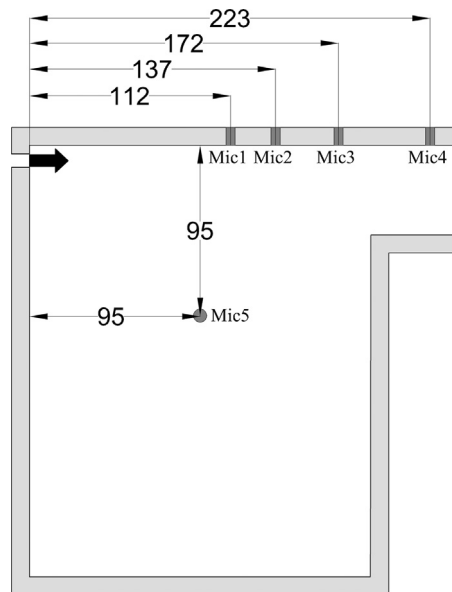


Fig. 6. Sketch of the experimental set-up adopted for the aeroacoustic measurements.

2.4. Static wall pressure measurements

The symmetry plane of the RPE model has been equipped with 23 static pressure taps 0.9 mm in diameter, placed along the top wall. The array begins 10 mm downstream of the RPE backward face, and the streamwise separation between two consecutive taps was 10 mm (measured from center to center) as reported in Fig. 5. An Airflow TSI PVM620 series pressure transducer was used to measure a differential pressure in the range -3735 Pa to 3735 Pa and a rotary scanivalve was implied to sequence the pressure ports.

2.5. Aeroacoustic measurements

Aeroacoustic measurements have been performed for several mass flow inlet. Five microphones flush mounted at wall have been installed as illustrated in Fig. 6. Microtech Gefell M360 microphones have been used, four of which flush-mounted on the RPE and one installed stand-alone, 100 mm far from the outlet. The microphone outputs were acquired using a National Instruments A/D board at 20 kHz for 60 s using an anti-aliasing cut-off frequency filter at 5 kHz. The mass flow inlet was varied between 7 g/s and 15 g/s, corresponding to a Re based on the inlet diameter ranging between about 2×10^4 and 5×10^4 . The aspect ratio was varied from 2.0 to 4.4 in order to obtain a total number of 36 more interesting geometries.

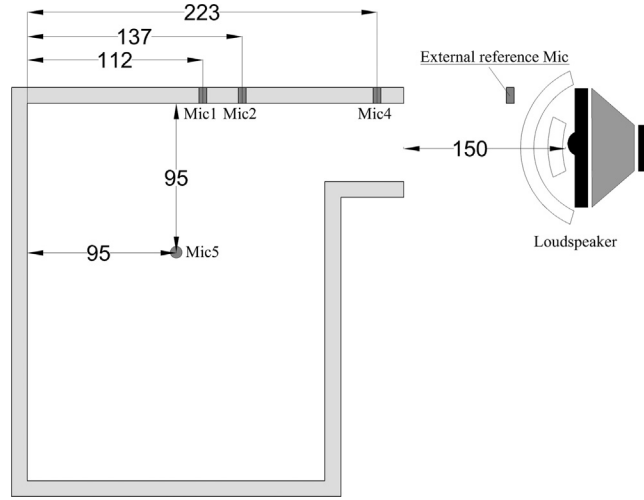


Fig. 7. Sketch of the experimental set-up adopted for the modal test.

2.6. Acoustic measurements

In a *stand-alone* configuration, in still air, the acoustic properties of the RPE have been preliminary tested through a modal test analysis carried out experimentally in a semi-anechoic chamber (see [21] for more details on the anechoic chamber). For the purpose of damping the vibration of the system, the model was supported by a tripod positioned on a sand-box. A loudspeaker, preliminarily characterized, was located 150 mm far from the outlet section, with the scope of forcing the acoustic modes of the test case. A sketch of this experimental set-up is shown in Fig. 7. The modal test has been performed by applying a swept-sine spanning from 100 Hz to 500 Hz and using the same measurement chain and acquisition parameters as the ones adopted for the described aeroacoustic measurements. As will be shown below, the spectral response is given in terms of the frequency response function (FRF_{SPL}) that is computed as follows:

$$FRF_{SPL} = \frac{L_{ps}^i}{L_{ps}^o} \quad (2)$$

where L_{ps}^o is the so-called reference *sound-pressure spectrum level* [22] computed from external reference microphone located outside of the test case, inside the anechoic chamber and in close proximity of the loudspeaker. Instead L_{ps}^i is determined inside the cavity using mic. 5. Varying D from 100 mm to 220 mm and d from 50 mm to 30 mm, 36 different cavity aspect ratios have been tested to determine accurately the dependence of the first mode frequency upon Γ .

3. Fluid dynamic characterization

The aerodynamic characterization provides an overall picture of the main flow structures forming within the cavity. A simplified sketch of the RPE flow physics is represented in Fig. 8. For all the aspect ratios analyzed herein, a few important flow structures have been identified: a free jet flow, a jet–wall interaction region, a large scale vortex, a recirculation bubble formed into the neck, a stagnation point. As described in Section 2.3, in order to describe with the proper spatial resolution all these flow behaviors, different FOV were adopted for the PIV measurements. Fig. 9(a) and (b) reports the averaged velocity field for a fixed mass addition equal to 15 g/s, for a cavity aspect ratio of 2.6 and 3.8 respectively. It can be observed that the fluid dynamic behavior is strongly affected by Γ . Indeed, despite the Γ variation inducing a weak modification of the vortex displacement, the vortex intensity varies significantly. In Fig. 9(c) and (d), the azimuthal, V_θ , and radial, V_r , velocity profiles, extracted along the x direction using the vortex center as a reference, are reported. It should be stressed that previous studies [23] demonstrated that the azimuthal velocity evolution influences the mixing and the main vortex stability into TVCs. It is noticeable that for the square cavity ($\Gamma=3.8$), the V_θ distribution is symmetric with respect to the vortex center and exhibits a linear trend in analogy with the inner zone of a Rankine vortex. This result suggests that the square cavity configuration traps the vortex in the most efficient way. Indeed, [11] experimentally investigated a geometry very similar to the present one but in reactive condition, and concluded that the square cavity configuration is the most efficient one in terms of combustion performances. Another interesting feature consists in the formation of a recirculation bubble in the neck. This effect is due to the presence of an adverse pressure gradient and it is observed for all the cases under consideration. The length scale and the position of this structure are affected by Γ , since this parameter influences the adverse pressure gradient intensity. In order to better characterize this feature, PIV measurements carried out in the FOV₂ have been analyzed. Results reported in Fig. 10(a) and (b), corresponding again to $\Gamma=2.6$ and 3.8, demonstrate that a

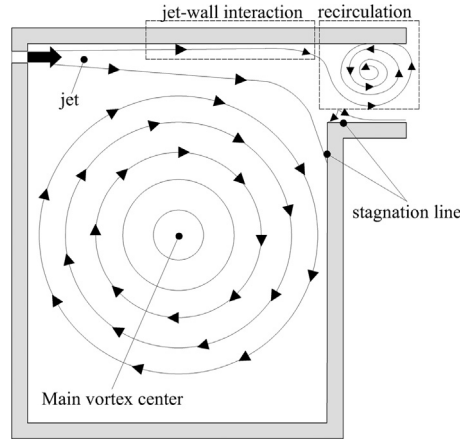


Fig. 8. Sketch of the flow physics.

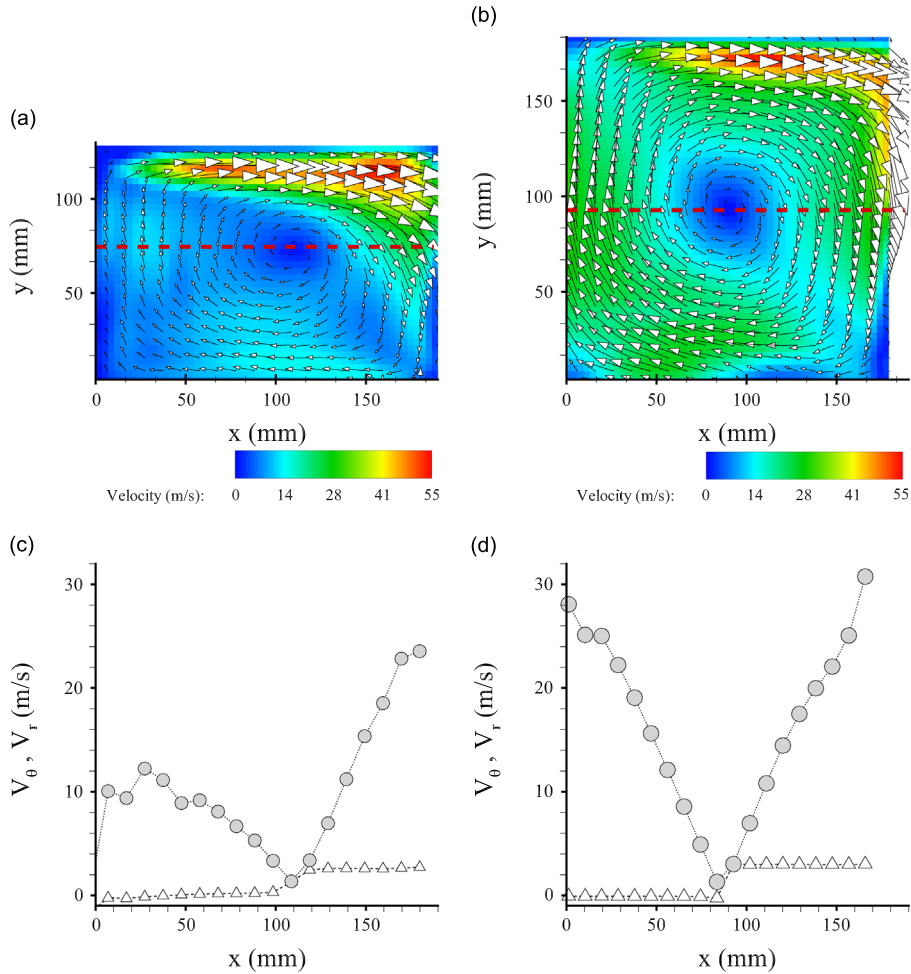


Fig. 9. Averaged velocity fields measured at $Re = 50\,271$ for different values of the cavity aspect ratio: $\Gamma = 2.6$ (a), $\Gamma = 3.8$ (b). Azimuthal (\circ) and radial (\triangle) velocity profiles extracted from the PIV data at $y = 73$ mm for $\Gamma = 2.6$ (c) and at $y = 90$ mm for $\Gamma = 3.8$ (d).

recirculation bubble is formed in the neck independent of the aspect ratio. The scale and the position of the recirculation region are strongly affected by Γ , its size being larger for larger Γ .

In order to better characterize the influence of Γ on the recirculation bubble intensity, the normalized mean static pressure, measured along the upper wall of the cavity model, has been analyzed. The results achieved for $\Gamma = 2.6$ and 3.8 are reported in Fig. 11. The data are reported in term of $Cp^* = (p_w - p_e) / \frac{1}{2} \rho U_{in}^2$, where p_w is the time averaged wall pressure, p_e is

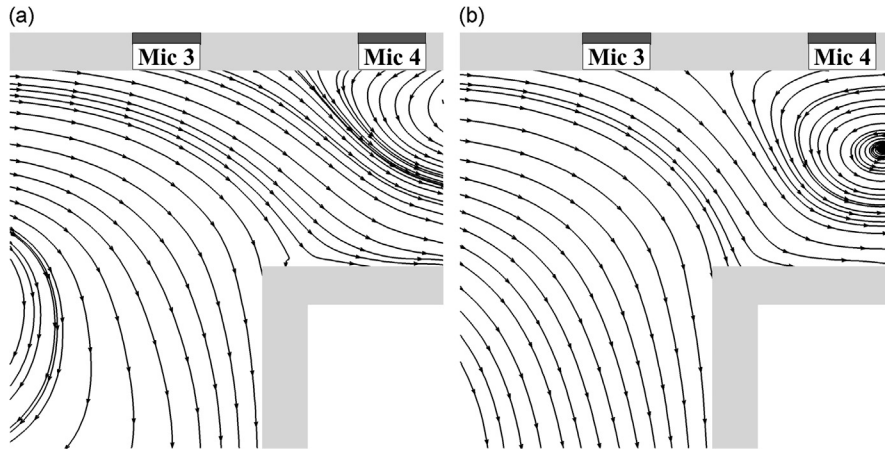


Fig. 10. Streamlines of the averaged velocity field, corresponding to FOV_2 and measured at $Re = 50\,271$ for $\Gamma = 2.6$ (a) and $\Gamma = 3.8$ (b).

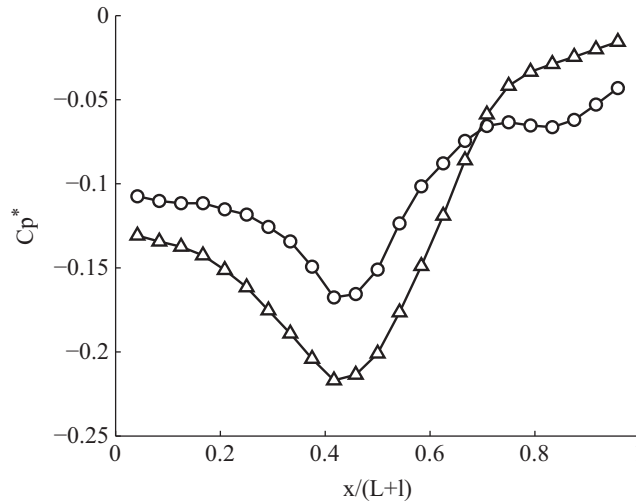


Fig. 11. Pressure coefficient distribution along the top wall of the RPE: (Δ) square cavity, (\circ) rectangular cavity.

a reference pressure, measured at the exit of the model, U_{in} is the mean flow velocity at the inlet and ρ is the fluid density. The streamwise distance is normalized with respect to the top wall length, i.e. $L+1$. It can be observed that the most intense vortex generated for $\Gamma = 3.8$ induces a relevant variation of pressure in the cavity and thus the largest adverse pressure gradient. In summary, a significant connection among the large scale dominant vortex intensity, the recirculation bubble properties and Γ , is evident. The results to be presented in the following shall demonstrate that the cavity aspect ratio affects significantly the wall pressure statistics as well as an effect of its influence upon the topology and intensity of the large scale flow structures.

4. Acoustic results

The acoustic modes in the *self-excited* condition are expected to influence significantly the wall pressure fluctuations even in the presence of a mean flow. For this reason, a detailed analysis of the acoustic response of the cavity has been carried out with the scope of determining quantitatively the typical frequencies of the acoustic resonances. A theoretical model has been developed to provide a prediction of the frequency of the first acoustic mode, and experiments and FEM numerical simulations have been performed to demonstrate its reliability. Those theoretical, numerical and experimental results are presented in the next subsections.

4.1. Acoustic numerical simulation

A three-dimensional finite element model of the present RPE, using the commercial software COMSOL, has been developed and solved in the frequency domain. The pressure distribution is provided over the frequency range 50–2000 Hz

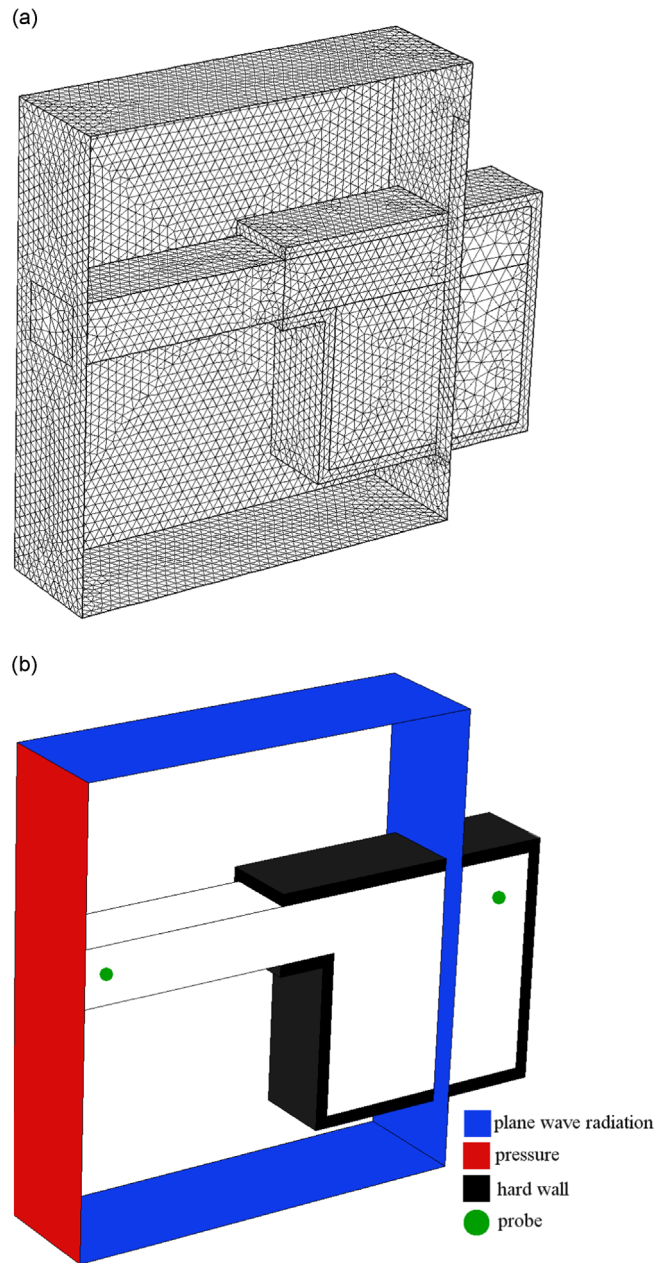


Fig. 12. Sketch of the mesh adopted (a); representation of the boundary conditions and the probe locations (b).

with a resolution of 1 Hz. All sides of the exterior domain surrounding the cavity have been modelled as open radiating into the free space. As acoustic forcing, a constant pressure has been imposed at the vertical wall of the external domain. Dissipative effects due to the viscous losses of the air moving back and forth in the neck have been neglected. A mesh refinement procedure has been applied in order to achieve solutions independent of the mesh size and a scheme of the mesh. The final mesh adopted after the refinement procedure is given in Fig. 12 (a). This configuration corresponds to 10^5 tetrahedral cells.

The boundary conditions assumed for the simulation and the probe points taken into account to compute the frequency response function, FRF_{SPL} , are illustrated in Fig. 12(b). FRF_{SPL} computed from the numerical simulations reported in Fig. 13 are analyzed to identify the frequencies of the modes that correspond to the peaks in the FRF_{SPL} . The first three modes achieved in the case of a square and a rectangular A cavity are reported in Figs. 14 and 15 respectively. In the square case, coalescence of the frequencies associated to the second longitudinal and transverse modes occurs. As a consequence the second mode, calculated by the FEM code, appears as a linear combination of longitudinal and transversal modes in

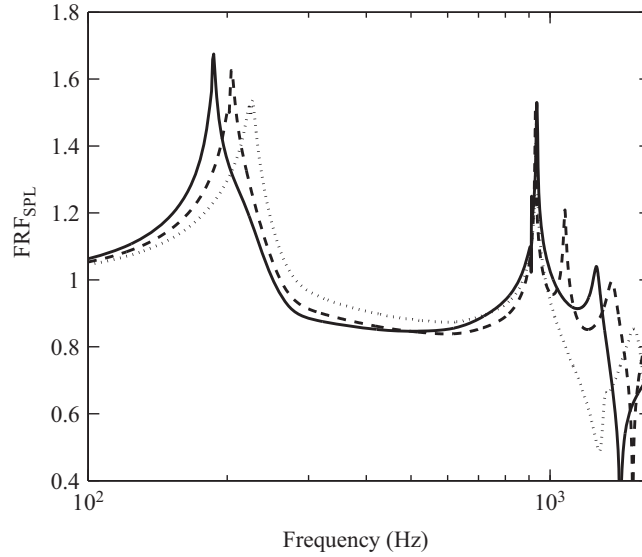


Fig. 13. Frequency response function for three different configurations: $\Gamma=3.8$ (—), $\Gamma=3.2$ (---), $\Gamma=2.6$ (····).

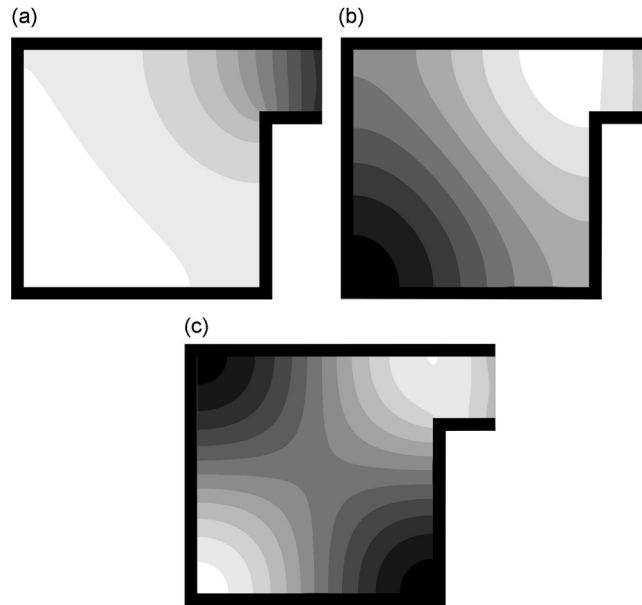


Fig. 14. First three modes occurring in the square RPE. Gray scale represents the sound pressure level in arbitrary scale.

[Fig. 14\(b\)](#). This combination is marked as *2LT*. The values of the modal frequencies obtained numerically are summarized in [Table 3](#). It is interesting to note that in the region close to the outlet section, a development of the first mode outside of the neck can be clearly observed (see [Fig. 16](#)). Such a result suggests that in order to predict correctly the mode frequencies using a plane wave model, an appropriate end correction has to be applied. This approach is presented in the next section.

4.2. Plane waves model and experimental results

The frequency of the first acoustic mode is predicted using a plane wave propagation model. The plane wave assumption is correct only for low frequency oscillations, a reasonable hypothesis when only the first mode is taken into account. As a further assumption, the medium in the system is assumed to be uniform and at rest. An acoustic lumped model can be established by decomposing the RPE into two regions separated by a section discontinuity. These regions are commonly indicated as cavity and neck (see [Fig. 17](#)). The general solution of the homogeneous wave equation, satisfying the hard-wall

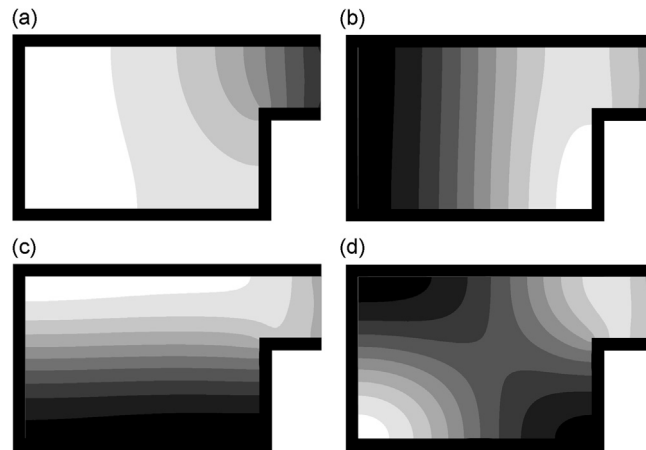


Fig. 15. First three modes occurring in the rectangular RPE: (a) first mode, (b) second longitudinal mode, (c) second transversal mode and (d) third mode. Gray scale represents the sound pressure level in arbitrary scale.

Table 3

First three mode frequencies varying Γ .

Γ	$1LT$ (Hz)	$2LT$ (Hz)	$2L$ (Hz)	$2T$ (Hz)	$3LT$ (Hz)
3.8	185	/	936	936	1273
3.2	202	/	935	1083	1378
2.6	225	942	/	1321	1534

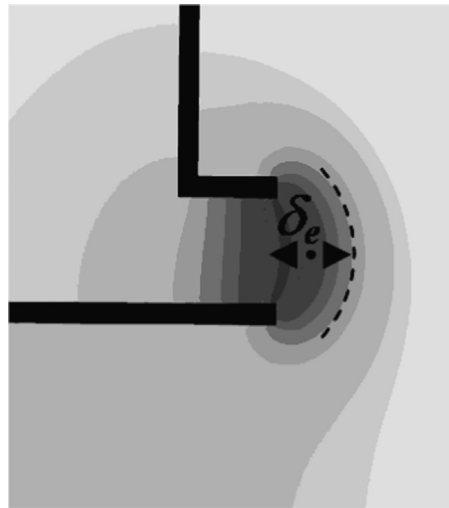


Fig. 16. Details of the exterior acoustic field simulated at the first mode frequency. The length of exterior end correction δ_e is qualitatively estimated and reported in the figure. The gray scale represents the sound pressure level in arbitrary scale.

and open-end boundary conditions, can be written in the following form:

$$\frac{1}{\Gamma} = \tan(kL) \tan(kl), \quad (3)$$

where k is the wavenumber, L the cavity length and l the neck length. Eq. (3) was found by [24] and applied by [25] to predict the frequency of the first acoustic mode of a so-called *double duct* geometry. A similar formulation has been suggested by [26] to predict the first acoustic mode of backward facing step geometries in combustors (see also [27]). A simplified resonant condition, corresponding to $kL \ll 1$ and $kl \ll 1$, can be derived from Eq. (3). By expanding this equation to the first order, the following conventional expression for the Helmholtz resonator (HR) is achieved:

$$\frac{1}{\Gamma} = k^2 L l. \quad (4)$$

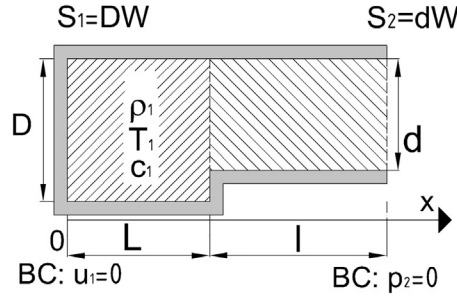


Fig. 17. Schematic representation of the lumped model.

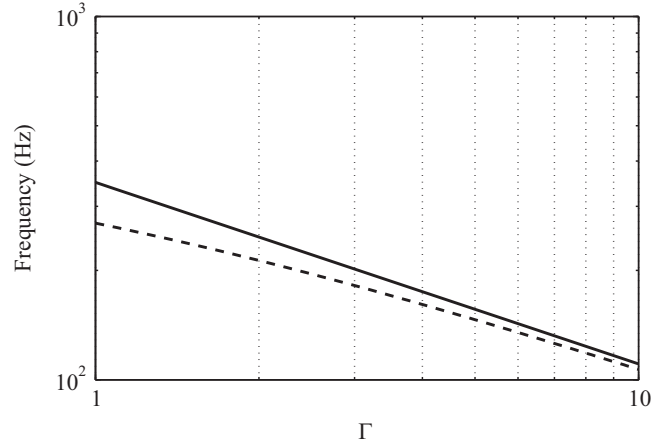


Fig. 18. Solutions of Eqs. (4) (cubical HR —) and (3) (double duct ---) obtained with Newton's method.

For both Eqs. (3) and (4), the wavenumber depends on the neck length, the cavity length and the cavity-neck section ratio, i. e. $k = f(\Gamma, L, l)$. By computing L and l for the present test model, the solution of Eq. (3) collapses well into Eq. (4). In Fig. 18 the departure of the solution of Eq. (3) from Eq. (4) is reported as a function of Γ . It is worth noting that despite the geometry under investigation being quite different from a cubical HR, with a centered and small orifice, its resonant behavior at high Γ can be represented well using the simple HR equation. The discrepancy observed at small Γ is related to the fact that the present simple model is based on the open-end boundary condition, $\hat{p}_2(L+l) = 0$. As was shown from the numerical results in Fig. 16, this assumption is not representing the actual physical behavior of the pressure at the outlet (see also [26]). As a consequence, in order to take into account the dependence upon time of the pressure at the outlet, an appropriate end-correction has to be introduced. From a formal viewpoint, the end-correction is commonly denoted as follows:

$$l' = l + \delta_e + \delta_i = l + 2\delta_R, \quad (5)$$

where δ_e and δ_i are exterior and interior end-corrections respectively. Therefore, Eq. (4) can be modified to obtain the following expression:

$$\frac{1}{\Gamma} = k^2 l', \quad (6)$$

The end-correction term commonly adopted in the literature is provided by the following expression:

$$l' = l + \delta_e + \delta_i = l + 2\delta_R = l + \alpha \sqrt{\frac{Wd}{\pi}}, \quad (7)$$

where $\sqrt{Wd/\pi}$ is the hydraulic radius of the neck [22]. The end-correction for axi-symmetric HR, expressed in dimensionless form, depends on the cavity-neck hydraulic diameters ratio and it ranges between two values, $0.785 < 2\delta_R/d < 0.848$ [28]. It has been checked that in the present case, these literature predictions do not lead to satisfactory results probably due to the peculiar neck shape and position in the present geometry. Hence a novel semi-empirical estimation of δ_R has been accomplished on the basis of our experimental results.

The experimental modal test performed allows us to calculate FRF_{SPL} that is reported in Fig. 19. The frequency and the amplitude of the first mode are strongly affected by Γ . In particular the amplitude of the mode increases significantly in the square cavity case. The dependence of the first mode frequencies upon Γ , determined by means of the experimental investigation, carried out for several Γ , is reported in Fig. 20 in a log-log scale. In this figure the typical Helmholtz resonator power law, $f \sim \Gamma^{-1/2}$, can be observed. Hence, despite the RPEs investigated being quite different from classical HR, it can be

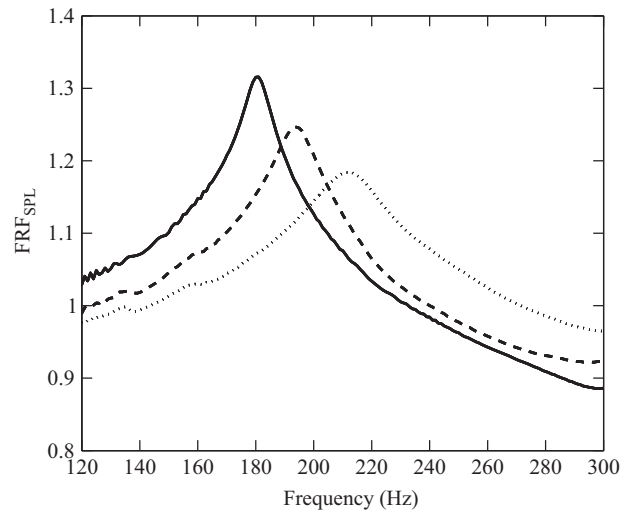


Fig. 19. Frequency response function for three different configurations: $\Gamma=3.8$ (—), $\Gamma=3.2$ (---) and, $\Gamma=2.6$ (·····).

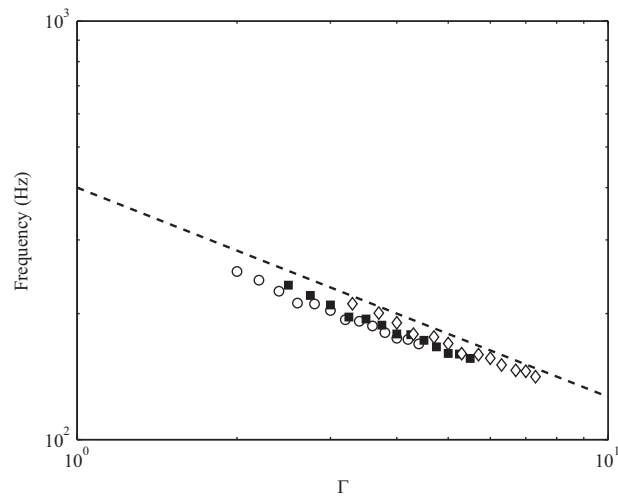


Fig. 20. First mode frequency referred to $d=50$ mm (\circ), $d=40$ mm (\blacksquare), $d=30$ mm (\diamond). The dashed line represents a power law decay with exponent $-1/2$.

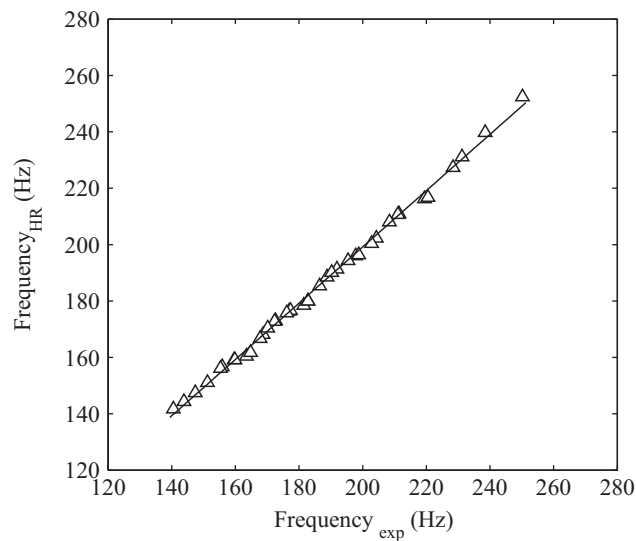


Fig. 21. Frequency of the first mode, measured experimentally, versus the frequency predicted applying the empirical end-correction modelled in Eq. (8). The linear fitting of the data is superimposed (—).

concluded that the first acoustic mode is exactly an HR mode. Whereas the weak frequency drifting, which occurs as a function of the transverse length of the neck, d , is due to the development of the first mode in the exterior domain, as was shown in Fig. 16. From a proper fitting of the experimental data, the following analytical expression of α is derived:

$$\alpha = \left[\frac{1}{L} \left(\frac{c}{2\pi 10^q} \right)^2 - l \right] \sqrt{\frac{\pi}{Wd}} \quad (8)$$

where q is the intercept of the linear fitting of the experimental data and its value is close to 2.55 for all the investigated cases. A comparison between the experimental frequencies and those predicted by the end-correction proposed in Eq. (8) is reported in Fig. 21, showing a very good agreement.

5. Wall pressure fluctuation statistics

In the presence of a flow, the acoustic pressure previously depicted is combined with the complex aeroacoustic behavior generated by the flow structures created inside the cavity. The estimated acoustic mode resonances as well as the velocity fields measured with the PIV technique provide a valid support to interpret the pressure data presented in both the physical and the Fourier domain. In the following subsections, single and multi-variate statistics are also presented. The achieved results provide an overall, reasonably clear picture of the relationship between the flow structures, the acoustic resonance and the wall pressure statistics, parameterized in terms of Γ and Re . We refer to Fig. 6 for the microphones numbering and positions.

5.1. Single-point statistics

The overall amplitude of the wall pressure fluctuations has been characterized through the computation of the root mean square pressure coefficient $C_{p_{rms}}$, defined as follows:

$$C_{p_{rms}} = \frac{\sigma_p}{\frac{1}{2}\rho U_{in}^2} \quad (9)$$

where σ_p represents the standard deviation of the pressure signal. As shown in Fig. 22 the largest pressure levels are measured in the cavity (microphones 1, 2, 3 and 5), whereas an important reduction occurs in the neck (microphone 4). A quite similar behavior is obtained for each Re investigated. The relevant reduction of $C_{p_{rms}}$ at mic. 4 location can be ascribed to reflections of the acoustic waves due to the section contraction sensed by the acoustic energy transmitted from the cavity to the neck. It is also interesting to note that, except for $\Gamma=2.6$ at the location of mic. 4, the $C_{p_{rms}}$ is weakly dependent upon Γ . In order to better clarify this behavior, the pressure fluctuations measured by mic. 4 are analyzed in more detail. The wall pressure power spectral density (PSD) measured by mic. 4 is reported in Fig. 23 for a fixed Re and different Γ . Except for the case at the lowest Γ , the shape of the spectra is similar in all cases, exhibiting a clear peak at the frequency of the first acoustic mode. The lowest Γ case is characterized by a larger energy content in the low frequency range that corresponds to the observed increase of the $C_{p_{rms}}$ magnitude. This behavior can be ascribed to the influence of the adverse pressure gradient induced in the neck that becomes significant in the lowest Γ case (see Fig. 11 for $0.8 < x/(L+l) < 1$). This aspect is further clarified by the analysis of the probability density functions (PDFs) of the pressure fluctuations measured by mic. 4 that are reported in Fig. 24 for different aspect ratios. The random variable is represented in reduced form in order to have

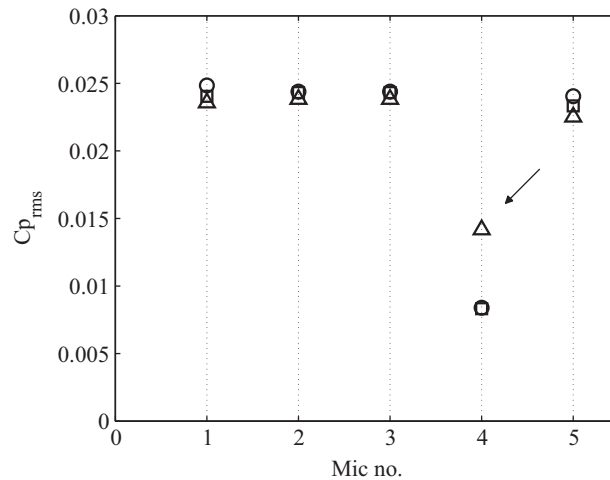


Fig. 22. $C_{p_{rms}}$ referred to all microphones and obtained for $Re = 50\,271$ and different aspect ratios: $\Gamma=3.8$ (□), $\Gamma=3.2$ (○) and $\Gamma=2.6$ (△). The arrow evidence the anomalous behavior of the microphone number 4.

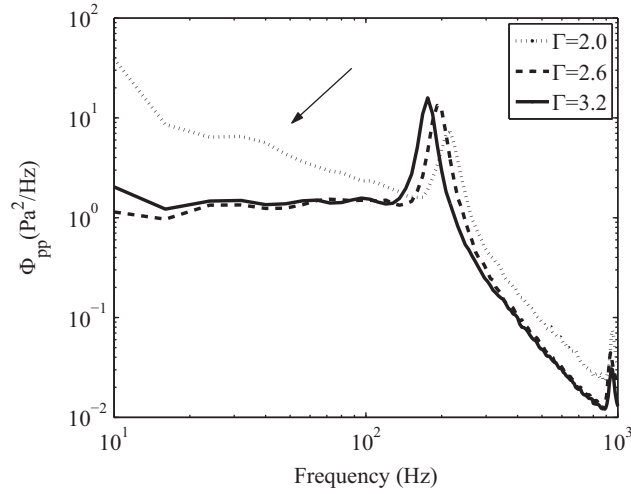


Fig. 23. Power spectral density referred to microphone 4 at $Re = 36\,865$ computed for $\Gamma = 3.8$ (—), $\Gamma = 3.2$ (---) and, $\Gamma = 2.6$ (·····).

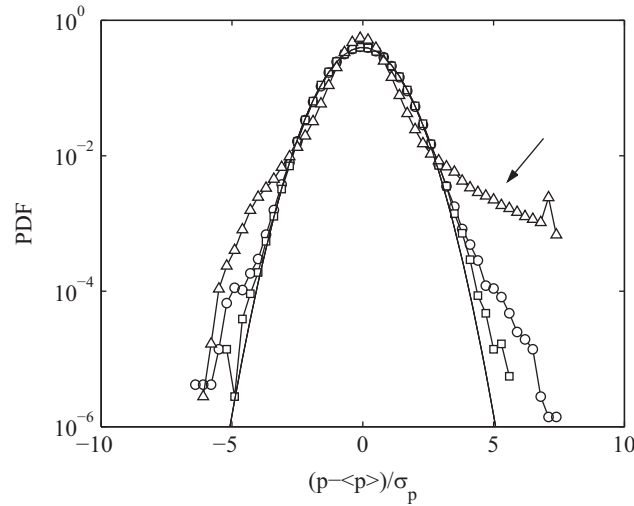


Fig. 24. Probability density function of pressure fluctuations measured by microphone 4 at $Re = 36\,865$ computed for $\Gamma = 3.8$ (\square), $\Gamma = 3.2$ (\circ) and $\Gamma = 2.6$ (\triangle).

zero mean and unitary standard deviation. The PDFs are all similar to the reference Gaussian curve except for the case at $\Gamma = 2.6$. More specifically, denoting with S the Skewness factor, it is found $S = 1.01$ for $\Gamma = 2.6$ and $S = 0.06$ for $\Gamma = 3.8$. The origin of such a behavior can be ascribed to the effect of random pressure surges, which are statistically relevant in the region of the neck, where they might be induced by the flow separation where a significant pressure gradient is present. To this extent, [29] observed a positive skewness of the wall pressure fluctuations in the reattaching zone of a separated region and interpreted this behavior as induced by inrush of irrotational flow towards the wall. A similar behavior has been found in the region of flow separation generated upstream of a forward-facing step [30]. An example of the effect of these surges in term of wall pressure fluctuations can be observed in Fig. 25, where several signatures with amplitude over $3\sigma_p$ can be detected. To confirm that high amplitude pressure fluctuations are related to the recirculation bubble dynamic, the proper orthogonal decomposition (POD) is applied to velocity field's domain Ω , which is indicated in Fig. 26. The POD is applied in this context to analyze the statistical properties of large-scale structures [31], in the present investigation generated within the neck. When most of the kinetic energy in the flow domain is embedded in a large-scale structure, a common outcome is that low-order modes determine the structure dynamics. In this work about 1200 snapshots have been used for the POD computations to ensure the convergence of the modes and the achieved results will be presented in the following. The POD eigenvalue's spectrum is reported in Fig. 27 and it is clear that an important part of the fluctuating energy is concentrated in the first mode. This result seems to be independent of Γ . As a consequence we can calculate the first-order POD expansion taking as approximation of the instantaneous flow field:

$$\mathbf{u}^n \approx \langle \mathbf{u}^n \rangle_N + a_1^n \Phi_1 \quad (10)$$

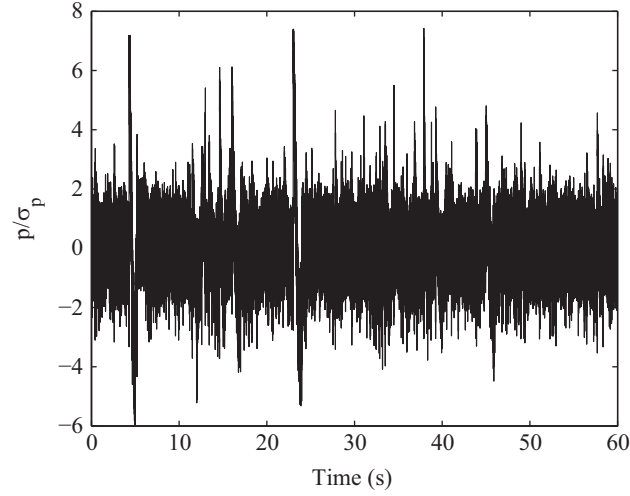


Fig. 25. Time history of pressure fluctuations normalized respect to its standard deviation and measured by microphone 4 at $Re = 36\,865$ and $\Gamma = 2.6$.

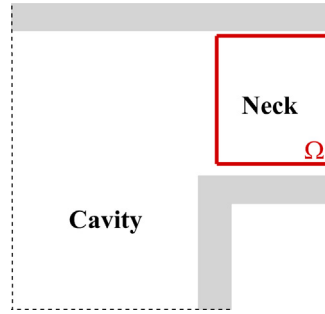


Fig. 26. Enlargement of the TVC geometry and POD domain representation.

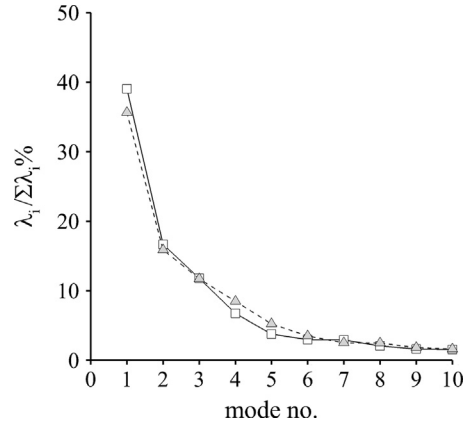


Fig. 27. Spectrum of the eigenvalues referred to $\Gamma = 2.6$ (□) and $\Gamma = 3.8$ (△).

where the operator $\langle \cdot \rangle_N$ represents the ensemble average, a_1 and Φ_1 the 1st POD coefficient and mode respectively. Furthermore, calculating the standard deviation of a_1 , denoted as σ_{a1} , the following term can be calculated:

$$\Theta_1 = \sigma_{a1} \Phi_1 \quad (11)$$

From statistical point of view, this term can be assumed as a model of the most intense perturbation induced by the first mode on the mean field. Hence, in a probabilistic sense, all instantaneous velocity fields can be assumed to be contained in

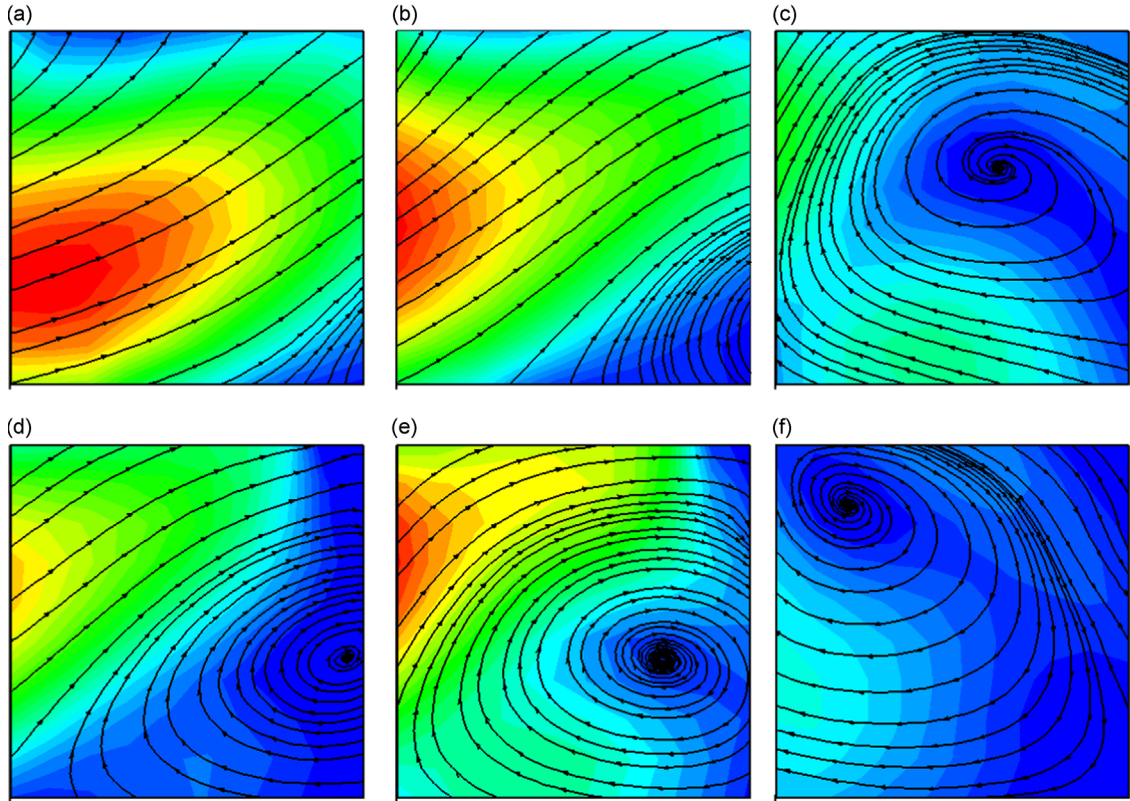


Fig. 28. Statistical reconstruction of the recirculation bubble dynamic using the first-order POD expansion, obtained for $\Gamma=2.6$ (a, b, c) and $\Gamma=3.8$ (d, e, f).

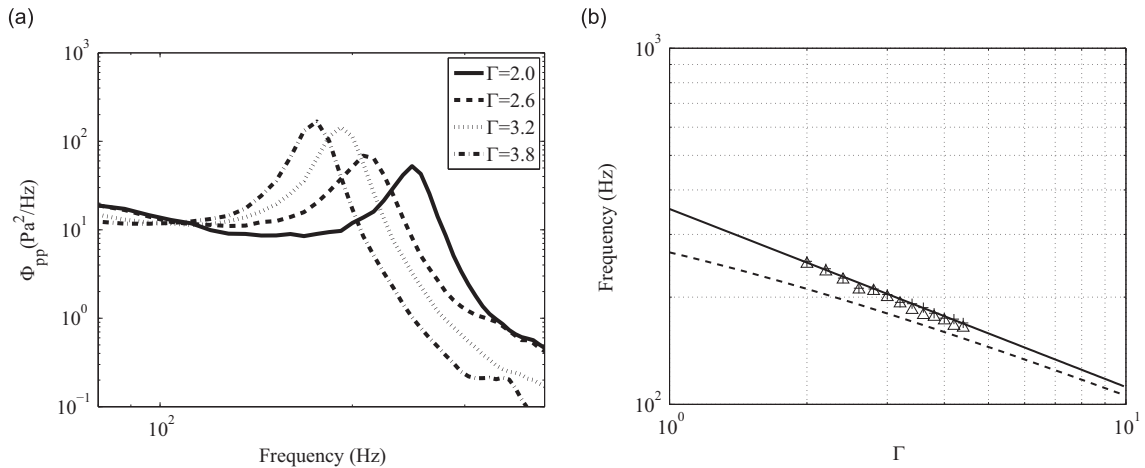


Fig. 29. Power spectral density referred to microphone 5 obtained varying Γ and keeping Re constant (a). First mode frequency, provided by means of the acoustic modal test (+) and aeroacoustic test (*), superimposed to solutions of Eq. (4) (cubical HR —) and Eq. (3) (double duct ---) (b).

the following range:

$$\mathbf{u}^n \in [\langle \mathbf{u}^n \rangle_N - \Theta_1; \langle \mathbf{u}^n \rangle_N + \Theta_1] \quad (12)$$

In Fig. 28, the three fields corresponding to $\langle \mathbf{u}^n \rangle_N - \Theta_1$, $\langle \mathbf{u}^n \rangle_N$ and $\langle \mathbf{u}^n \rangle_N + \Theta_1$ are reported for the rectangular and the square cavity (first and second row respectively). As can be observed for the geometry based on rectangular cavity the dynamic of the recirculation bubble is relevant and the large scale flow structure does not seem to be located within the neck. This unsteady behavior can be the source of the low frequency pressure surges, highlighted previously by observing the PSDs,

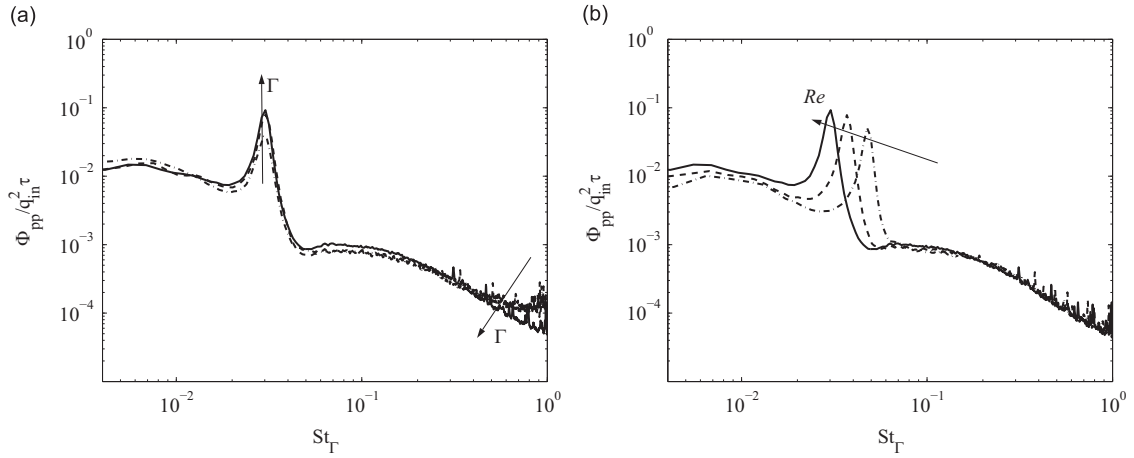


Fig. 30. Power spectral density of the wall pressure referred to microphone 1, the pressure is normalized by q_{in}^2 . The data are taken at $Re = 50\,271$ and $\Gamma = 2.6, 3.2$ and 3.8 (a). The data are computed at $Re = 50\,271, 36\,865, 30\,163$ and $\Gamma = 3.8$ (b).

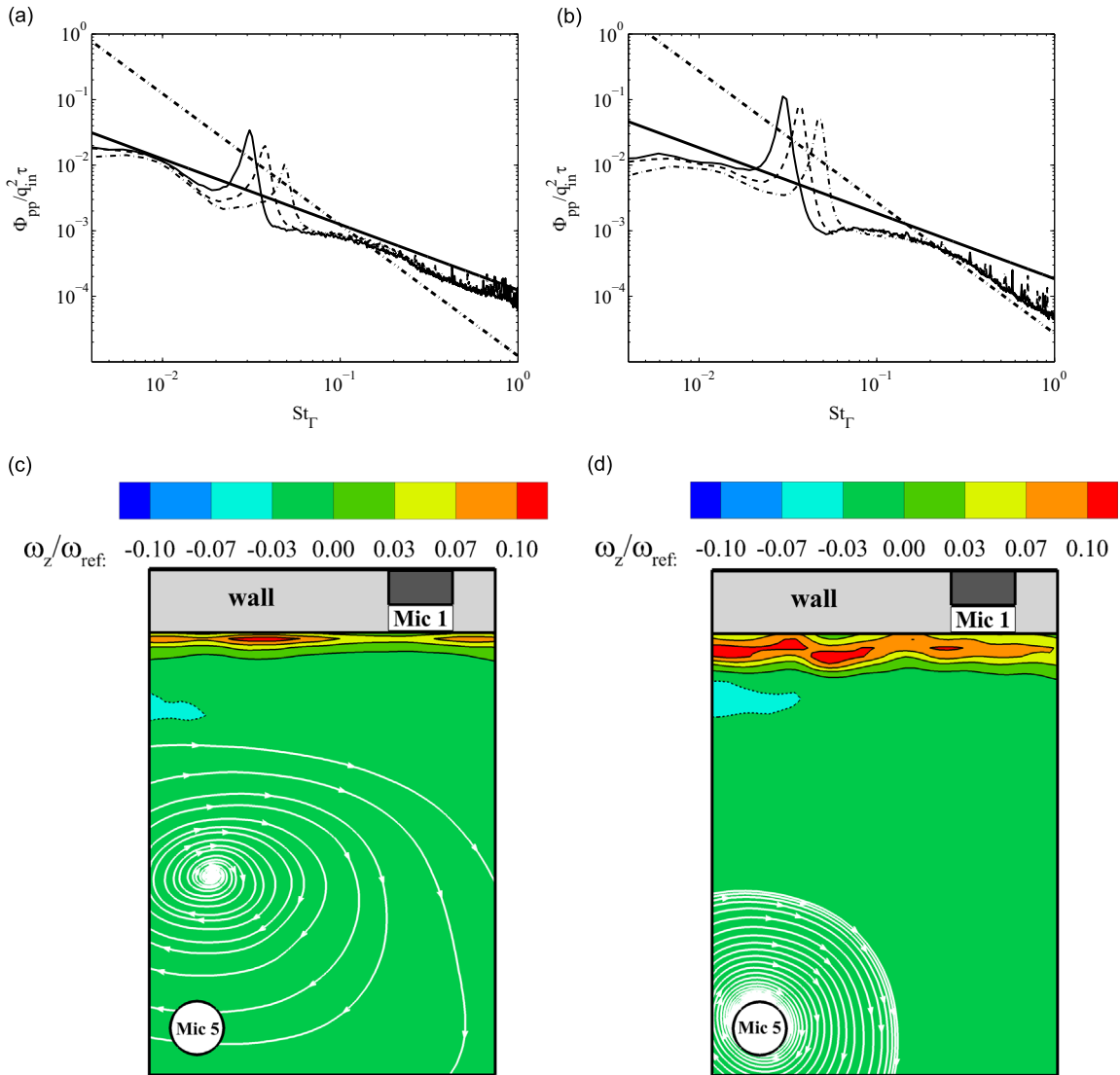


Fig. 31. Normalized power spectral density referred to microphone 1 for $Re = 50\,271$ (—), $Re = 36\,865$ (---) and $Re = 30\,163$ (- · -). Spectra calculated for rectangular and square cavities are reported in (a) and (b). The solid line represents the slope -1 whereas the dash-dotted line the slope -2 . Cases (c) and (d) report contour plots and streamlines of the averaged vorticity field in the case of $Re = 50\,271$ calculated for two values of cavity aspect ratio: $\Gamma = 2.6$ (c) and $\Gamma = 3.8$ (d).

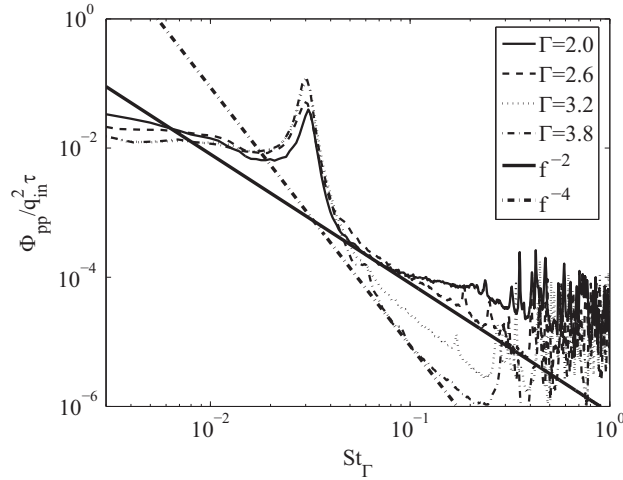


Fig. 32. Normalized power spectral density referred to microphone 5 for different Γ and $Re = 50\,271$.

PDFs and the time history of the wall pressure. As pointed out above, the wall pressure PSDs are influenced significantly by the acoustic mode. Indeed, the acoustic resonance affects the overall pressure dynamics and it is sensed by the whole set of microphones used in the present experiment. As a matter of fact, the spectra reported in Fig. 29(a) clearly show a peak at about the same frequency as that of the first acoustic mode determined by the acoustic numerical and experimental investigations. The acoustic nature of these peaks is demonstrated by Fig. 29(b) where those frequencies are compared both to the analytical predictions obtained by the solution of Eqs. (3) and (4) and experimental frequencies measured by means of the modal test. According to the acoustic analysis of Section 4, the experimental data are in fairly good agreement with the scaling law predicted by the simple HR model and reported in the following:

$$f = \frac{c_0}{2\pi} \sqrt{\frac{1}{\Gamma L}} \rightarrow f \propto \Gamma^{-1/2}, \quad (13)$$

The above results clearly show that the parameter Γ influences significantly the largest peaks of the pressure spectra. Taking into account this consideration, in order to scale appropriately the low frequency range of the pressure spectra, the frequency can be normalized as follows:

$$St_\Gamma = \frac{f d_{in}}{U_{in}} \Gamma^{1/2}, \quad (14)$$

where U_{in} is the mean inlet velocity and d_{in} the inlet section diameter. St_Γ is a *reduced* Strouhal number that takes into account the variation of Γ and, as shown in Fig. 30, leads the spectra to collapse very well in the low frequency range. In the plot of Fig. 30, the y-axis is normalized with respect to the inlet dynamic pressure (q_{in}) and using the local reference time $\tau = d_{in}/U_{in}$. The effect of Re is reported in Fig. 30(b) where it can be observed that a collapse of the peaks is no longer observed whereas the spectra collapse well in the high frequency range. In order to investigate the high frequency behavior at large St ($St_\Gamma > 0.5$) the PSDs for $\Gamma=2.6$ and $\Gamma=3.8$, computed at three different Re , are reported in Fig. 31(a) and (b). Two different power law decays, with exponents -1 and -2 , are highlighted by the straight lines in the log–log representation. The -1 power law is observed at $\Gamma=2.6$ and it is characteristic of equilibrium turbulent boundary layers (TBLs), associated with turbulent activity in the log layer [32]. On the other hand, a power decay equal to -2 is typical of *non-equilibrium* TBL and is observed to apply in the rectangular cavity case ($\Gamma=2.6$). Na and Moin [33] performed a DNS of a TBL developing over a flat plate, and a power law decay with exponent close to -2 was observed for the spectra downstream of a reattachment location. With reference to Fig. 11, the APG at the location of mic. 1 (that is for $x/(L+l) = 0.46$) is larger for $\Gamma=3.8$ than for $\Gamma=2.6$. The PIV results reported in Fig. 31(c) and (d) also support this interpretation. In fact it is observed that the vorticity shear close to the wall, in the square cavity case, appears thickened and more irregular than in the rectangular one thus suggesting that the wall flow in the second case is closer to a regular TBL. The pressure spectra computed from the transverse microphone (mic. 5) are reported in Fig. 32 for different aspect ratios. In this case, the exponent of the spectral scaling in the high frequency range varies from -2 to -4 for increasing Γ . This behavior explained through the vorticity fields provided by the PIV measurements is in dimensionless form ω_z/ω_{ref} , where $\omega_{ref} = 1/\Delta t$ and Δt is the time delay between two consecutive laser pulses. Fig. 31(d) clearly shows that for $\Gamma=3.8$ the large scale vortex core is centered on mic. 5. Indeed, as pointed out e.g. by [33] the power law exponent -4 is typical of a separation bubble. On the other hand, as shown in Fig. 31(c), a variation of the cavity aspect ratio from $\Gamma=3.8$ to $\Gamma=2.6$ corresponds to a relevant displacement of the vortex core thus explaining the power law variation from -4 to -2 .

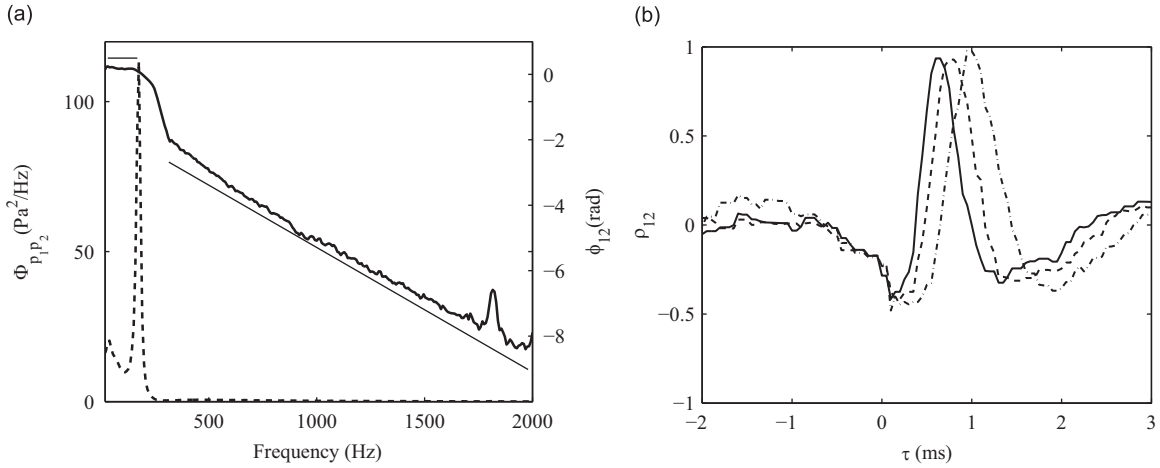


Fig. 33. Cross-spectrum magnitude (---) and phase (—) (a). Cross-correlation between microphones 1 and 2 computed after filtering the raw signals with high-pass filter, the curves are provided for three different Re numbers: 50 271 (—), 36 865 (---) and 30 163 (-·-) (b).

Table 4

The convection velocity and the convection-inlet velocity ratio are gathered in this table for square and rectangular cavities at different Re numbers.

Γ	Re	U_c (m/s)	U_c/U_{in}
3.8	30 163	23.6	0.48
3.8	36 865	29.1	0.46
3.8	50 271	37.7	0.49
2.6	30 163	24.8	0.50
2.6	36 865	32.9	0.52
2.6	50 271	38.0	0.49

5.2. Two-point pressure statistics

The simultaneous measurement of pressure by several wall mounted microphones allows for the computation of cross-correlations and cross-spectra that are crucial quantities to be analyzed for the characterization of the propagation of the pressure perturbations. Indeed, the analysis of pointwise signals presented in the previous section suggests that the low frequency phenomena are dominated by acoustic resonances leading to the generation of acoustic waves propagating at the speed of sound. On the other hand, higher frequencies seem to be influenced by the large and small scale flow structures, localized in the bulk and close to the wall and inducing hydrodynamic pressure fluctuations. The convection velocity U_c is directly dependent upon the nature of the pressure perturbations. According to e.g. [34], it is possible to define U_c through the cross-spectral phase ϕ_{ij} computed between a couple of sensors separated by a distance ξ , as follows:

$$\phi_{ij} = \frac{\omega \xi}{U_c(\omega, \xi)} \quad (15)$$

The cross-spectral magnitude and phase, computed between mics. 1 and 2, is displayed in Fig. 33(a) for the square cavity case. The phase exhibits a plateau at low frequencies and a decaying region with a negative slope at higher frequencies. The first one ranges from 10 Hz up to the frequency of the first acoustic mode, the second one ranges from the first mode frequency up to around 2000 Hz. The plateau can be ascribed to the acoustic effect since all pressure time scales propagate at the same velocity. On the other hand, according to the definition provided in Eq. (15), the negative slope can be interpreted to be a consequence of convective effects. This interpretation is confirmed by the analysis of the cross-correlation between the signals measured by mics. 1 and 2 and properly filtered in advance. More specifically, a second-order Butterworth high-pass filter using a frequency cut-off of 200 Hz has been applied. All signals are processed synchronously, to avoid the occurrence of phase drift across the records from different microphones. In this way, the acoustic resonance is excluded and only high frequencies, that are supposed to be associated to the hydrodynamic pressure, are considered. The cross-correlations between the filtered signals are reported in Fig. 33(b), where can be observed that the time delay, τ , associated to the peak of the correlations vary with Re . This result according to the cross-spectra phase can be ascribed to the hydrodynamic advection. This analysis allows us the computation of the hydrodynamic convection velocity, $U_c = \xi/\tau$, whose values, for different Γ , are summarized in Table 4. It can be observed that the ratio between U_c and the velocity inlet is about constant and equal to 0.5, furthermore it is not affected neither by Γ nor by Re .

6. Concluding remarks

The acoustic and the aeroacoustic behavior of a RPE have been studied by applying several experimental measurement techniques and an acoustic numerical simulation. The fluid dynamic field for different geometrical configurations has been characterized using the PIV technique. The aerodynamic study evidenced the main flow structures, including separations bubbles near the walls and a large scale vortex in the bulk and it has been verified that the square cavity geometry is the best in terms of large scale vortex intensity. From the acoustic view point it has been highlighted that RPE behaves as a Helmholtz resonator, and a novel end-correction formula has been proposed and validated against experimental data. Further a prediction model based on Helmholtz Resonator formulation and on a novel end-correction has been derived. The aeroacoustic measurements have shown that the first acoustic mode dominates the wall pressure spectra also in the presence of a mean flow. A reduced form of *Strouhal* number has been proposed on the basis of the frequency scaling of the first acoustic mode and a good collapse of the frequency spectra in low frequency range has been achieved. On the other hand, it has been shown that the high frequency region of the spectra is affected by the APG that influences the jet–wall interaction and induces a non-equilibrium condition of the flow close to the wall. This behavior induces a variation of the high frequency spectra slope, from -1 to -2 . The recirculation region has been characterized also through a POD decomposition of the PIV velocity fields. It is found that the dynamics of the bubble formed into the neck depends on Γ , leading the pressure fluctuations to increase at low frequencies. The results provided in the present investigation definitely demonstrate that the main parameter to be taken into account in the design of this kind of geometry is the cavity–neck aspect ratio.

Acknowledgments

This research has been supported by Ministero dello Sviluppo Economico - Ricerca di Sistema Elettrico. The authors wish to thank ENEA represented by Eng. S. Giammartini for his support to this activity. Eng. M. Liani and D. Zucconi are also acknowledged for their support during the measurement campaign and Dr. E. Stefanutti for helpful discussion about mathematical modelling.

References

- [1] B. Venkatesham, M. Tiwari, M.L. Munjal, Transmission loss analysis of rectangular expansion chamber with arbitrary location of inlet/outlet by means of Green's functions, *Journal of Sound and Vibration* 323 (2009) 1032–1044.
- [2] S. Ziada, Flow-excited acoustic resonance in industry, *Journal of Pressure Vessel Technology* 132 (2010) 1–9.
- [3] J.C. Bruggeman, A. Hirschber, M.E.H.V. Dongen, A.P.J. Wijnands, Self-sustained aero-acoustic pulsations in gas transport systems: *experimental study of the influence of closed side branches*, *Journal of Sound and Vibration* 150 (1991) 371–393.
- [4] C.K.W. Tam, The acoustic modes of two-dimensional rectangular cavity, *Journal of Sound and Vibration* 49 (1976) 353–364.
- [5] C.K.W. Tam, P.J.W. Block, On the tones and pressure oscillations induced by flow over rectangular cavities, *Journal of Fluid Mechanics* 89 (1978) 373–399.
- [6] N. Murray, E. Sällström, L. Ukeiley, Properties of subsonic open cavity flow fields, *Physics of Fluids* 21 (2009) 353–364.
- [7] J.J. Keller, Nonlinear self-excited acoustic oscillations within fixed boundaries, *Journal of Fluid Mechanics* 123 (1982) 267–281.
- [8] J.J. Keller, M.P. Escudier, Flow-excited resonances in covered cavities, *Journal of Sound and Vibration* 86 (1983) 199–226.
- [9] J.J. Keller, Non linear self-excited acoustic oscillations in cavities, *Journal of Sound and Vibration* 94 (1984) 397–409.
- [10] R.C. Hendricks, D.T. Shouse, W.M. Roquemore, D.L. Burrus, B.S. Duncan, R.C. Ryder, A. Brankovic, N.-S. Liu, J.R. Gallagher, J.A. Hendricksand, J. A. Hendricks, Experimental and computational study of trapped vortex combustor sector rig with high-speed diffuser flow, *International Journal of Rotating Machinery* 7 (2001) 375–385.
- [11] A. Singhal, R.V. Ravikrishna, Single cavity trapped vortex combustor dynamics—Part-1: *experiments*, *International Journal of Spray and Combustion Dynamics* 3 (2011) 23–44.
- [12] A. Singhal, R.V. Ravikrishna, Single cavity trapped vortex combustor dynamics—Part-2: *simulations*, *International Journal of Spray and Combustion Dynamics* 3 (2011) 45–62.
- [13] K.Y. Hsu, C.D. Carter, V.R. Katta, W.M. Roquemore, Characteristics of combustion instability associated with trapped vortex burner, *19th AIAA Aerospace Science Meeting and Exhibit*, Reno, NV 99-0488, 1999, pp. 1–9.
- [14] K.K. Agarwal, R.V. Ravikrishna, Flow-acoustic characterisation of a cavity-based combustor configuration, *Defence Science Journal* 61 (2011) 523–528.
- [15] E.J. Gutmark, C. Paschereit, D.G.A. Lacarelle, J.P. Moek, S. Schimek, T. Faustmann, M.R. Bothein, Combustion noise in a flameless trapped-vortex reheat burner (ftvr), *13th AIAA/CEAS*, Rome, 2007.
- [16] K.S. Chang, S.O. Park, Hybrid rans/les simulation of deep cavity flow, *AIAA Paper* 53 (2004) 2004.
- [17] T. Pagliaroli, R. Camussi, Acoustic and aeroacoustic characterization of rectangular partial enclosures, *19th AIAA/CEAS*, Berlin, 2013.
- [18] C. Bogey, O. Marsden, C. Bailly, Effects of moderate Reynolds numbers on subsonic round jets with highly disturbed nozzle-exit boundary layers, *Physics of Fluids (1994–present)* 24 (10) (2012) 105107.
- [19] C.J. Wu, X.J. Wang, H.B. Tang, Transmission loss prediction on a single-inlet/double outlet cylindrical expansion-chamber muffler by using the modal meshing approach, *Applied Acoustics* 69 (2008) 173–178.
- [20] M. Stanislas, K. Okamoto, C.J. Kähler, J. Westerweel, F. Scarano, Main results of the third international PIV challenge, *Experiments in Fluids* 45 (2008) 27–71.
- [21] S. Grizzi, R. Camussi, Wavelet analysis of near-field pressure fluctuations generated by a subsonic jet, *Journal of Fluid Mechanics* 68 (2012) 93–124.
- [22] A.D. Pierce, *Acoustics*, Acoustical Society of America, 1994.
- [23] C. Bruno, M. Losurdo, The trapped vortex combustor: an advanced combustion technology for aerospace and gas turbine applications, *Advanced Combustion and Aerothermal Technologies*, 2007, pp. 365–384.
- [24] P.K. Tang, W.A. Sirignano, Theory of generalized Helmholtz resonator, *Journal of Sound and Vibration* 26 (2) (1973) 247–262.
- [25] T. Poinso, D. Veynante, *Theoretical and Numerical Combustion*, Edwards, 2005.
- [26] H.M. Altay, D.E. Hudgins, R.L. Speth, A.F. Ghoniem, Flame–vortex interaction driven combustion dynamics in a backward-facing step combustor, *Combustion and Flame* 156 (2009) 1111–1125.
- [27] H.M. Altay, D.E. Hudgins, R.L. Speth, A.F. Ghoniem, Mitigation of thermoacoustic instability utilizing steady air injection near the flame anchoring zone, *Combustion and Flame* 157 (2010) 686–700.

- [28] A. Selamet, P.M. Radavich, N.S. Dickey, J.M. Novak, Circular concentric Helmholtz resonator, *The Journal of the Acoustical Society of America* 101 (1997) 41–51.
- [29] M. Kiya, K. Sasaki, Structure of a turbulent separation bubble, *Journal of Fluid Mechanics* 137 (1983) 83.
- [30] R. Camussi, M. Felli, F. Pereira, G. Aloisio, A. DiMarco, Statistical properties of wall pressure fluctuations over a forward-facing step, *Physics of Fluids* 20 (2008) 075113.
- [31] S. Maurel, J. Borée, J. Lumley, Extended proper orthogonal decomposition: application to jet/vortex interaction, *Flow, Turbulence and Combustion* 67 (2001) 125–136.
- [32] P. Bradshaw, Inactive motion and pressure fluctuations in turbulent boundary layers, *Journal of Fluid Mechanics* 30 (1967) 241–258.
- [33] Y. Na, P. Moin, The structure of wall-pressure fluctuations in turbulent boundary layers with adverse pressure gradient and separation, *Journal of Fluid Mechanics* 377 (1998) 347–373.
- [34] G.M. Corcos, The structure of the turbulent pressure field in the boundary-layer flows, *Journal of Fluid Mechanics* 18 (1964) 353–378.